ACS APPLIED NANO MATERIALS

www.acsanm.org Article

Magnetic Nanowire Biolabels Using Ferromagnetic Resonance Identification

Joseph Um,* Yali Zhang, Wen Zhou, Mohammad R. Zamani Kouhpanji, Cosmin Radu, Rhonda R. Franklin, and Bethanie J. H. Stadler*

Cite This: *ACS Appl. Nano Mater.* 2021, 4, 3557−3564 Read Online

ACCESS | Metrics & More | Article Recommendations | Supporting Information

ABSTRACT: Nanomaterials have attracted attention from a variety of fields. For example, magnetic nanowires (MNWs) can be used to identify and/or distinguish objects using their magnetic signatures: first-order reversal curves, hysteresis curves, angle-dependent coercivity, and ferromagnetic resonance (FMR). Among these, FMR is the fastest measurement, and it shows the potential to identify many high-frequency signatures simultaneously. In this work, iron, cobalt, and nickel MNW samples are fabricated by template-assisted pulsed electrodeposition and are measured individually and in combination using an FMR-identification (FMR-ID) labeling system. The FMR-ID system is then optimized using the FMR measurement results, the original and revised Kittel equations, and the magnetic properties of the MNWs. The most efficient FMR-ID systems will use DC bias fields (0−15 kOe) that are parallel to the nanowires and microwave frequencies of 20 GHz or above. These MNW-based FMR-ID labeling systems will be effective wherever small identification markers are needed.

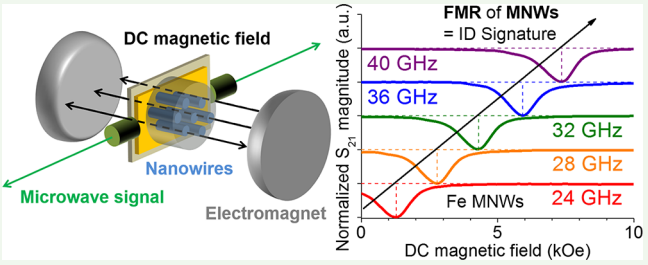

KEYWORDS: *magnetic nanowires, ferromagnetic resonance, identification, labeling, biolabels, electrodeposition, microwave absorption*

INTRODUCTION

The ubiquitous application of radio-frequency identification (RF-ID) has recently reached nanodimensions.[1−3] Nano-identification markers would be a useful addition to nanomaterials already in use in a variety of fields, including drug delivery,[4,5] hyperthermia therapy,[5,6] cell manipulation,[7,8] cell separation,[9] cryopreservation,[10−13] ferrogels,[14] and circulators in high-frequency circuits.[15] Magnetic nanowires (MNWs) in particular have shown promise for labeling cells for a specific therapy,[16−22] and these MNWs can have unique magnetic signatures to identify and/or distinguish the cells in an assay.[21−23] For read-out, first-order reversal curve (FORC) analysis has been shown to distinguish mixtures of two types of nickel MNWs with a high accuracy.[22] Other techniques that are excellent for characterization, such as hysteresis curves and angle-dependent coercivity,[19,24] do not detect individual signatures well, and FORC measurements are slow unless the projection method or backfield remanence is used.[25] Faster measurements are being explored, including ferromagnetic resonance (FMR) which has potential to identify many high-frequency signatures simultaneously.[23]

FMR measurements of magnetic nano- and microwires have been used to study magnetization dynamics for both fundamental and applied research.[26−47] However, FMR has merely been used as a measurement technique to date. Recently, Zhou et al. introduced FMR readout of MNWs as biolabels using the broadband FMR technique (also called the vector network analyzer (VNA)-FMR technique) based on coplanar waveguides (CPWs) with a focus on a fitting algorithm for detecting multiple MNW types using a mathematical model.[23] For FMR measurements, generally microwave circuit structures such as waveguide cavities, microstrips, and CPWs are used to provide an ac magnetic field induced from the microwave signal.[23,30,42,44,47] CPWs enable FMR measurements with a broad frequency range and easily accommodate rapid and multiple measurements of unknown samples compared to waveguide cavities, and CPWs produce a stronger ac magnetic field at the sample location which is more suitable for nanowire characterization than microstrips.[47] Here, FMR is utilized as the identification signature, and an FMR identification (FMR-ID) system is optimized using the broadband FMR technique together with carefully engineered magnetic properties of the MNWs themselves. Beyond cell labeling, these MNWs could prove useful wherever small identification markers are desired.

Received: January 11, 2021
Accepted: March 10, 2021
Published: March 26, 2021

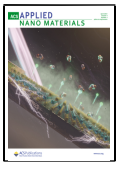

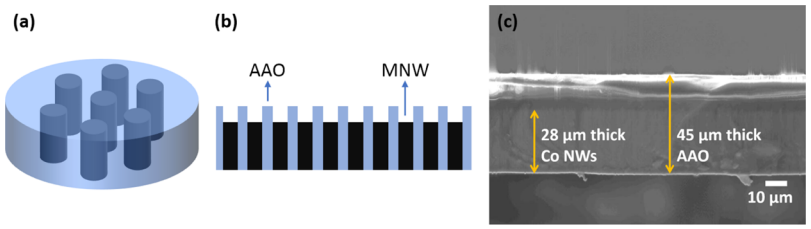

Figure 1. (a) Schematic and (b) cross section of AAO with MNWs. (c) SEM image of cross section of AAO with Co MNWs. Note that the bright spots are due to charging, which occurs after a darker (Debye) region above the MNWs.

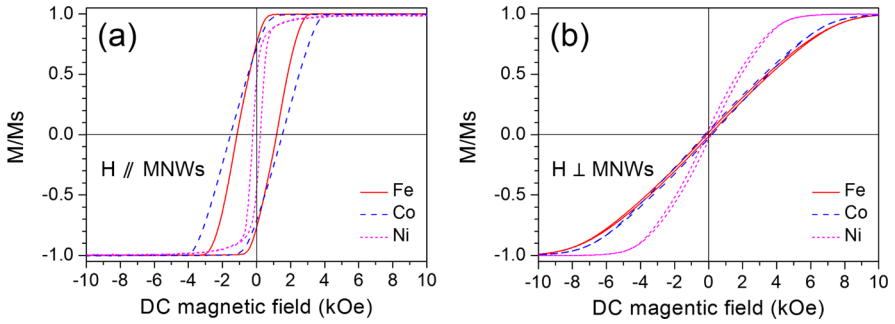

Figure 2. Hysteresis loops of Fe, Co, and Ni MNWs with the applied DC magnetic field (a) parallel and (b) perpendicular to the MNW axes.

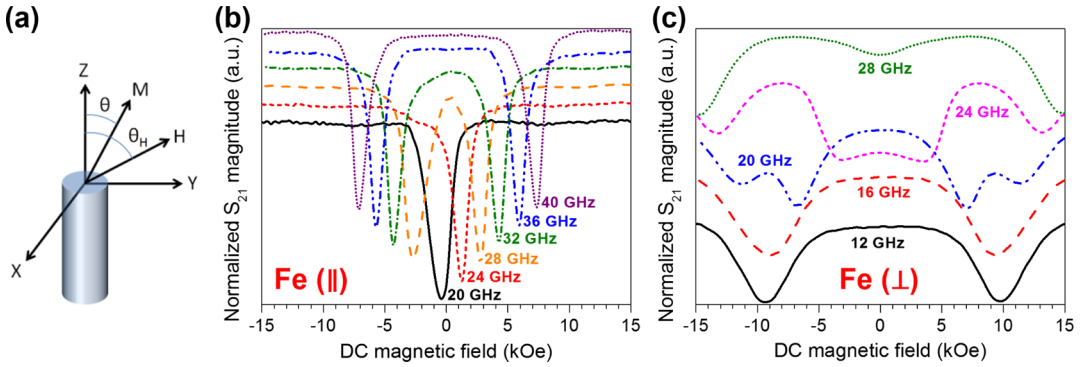

Figure 3. (a) Schematic defining the angles (θ) of magnetization (M) of a MNW and an applied field (H) relative to the MNW axis (z). (b,c) Stacked normalized S_{21} (microwave signal at the output compared to the input) at labeled frequencies for Fe MNWs with the DC field (b) parallel and (c) perpendicular to the MNW axis. Representative curves are shown here for clarity, and others are given in the Supporting Information.

RESULTS AND DISCUSSION

Nanowire Characterization. Iron (Fe), cobalt (Co), and nickel (Ni) MNWs were fabricated using AAO templates (for Fe and Co, 40 nm pore diameter, 12% porosity, and 50 μm thickness) and a TEPC membrane (for Ni, 200 nm pore diameter, 9% porosity, and 10 μm thickness) by pulsed electrodeposition. The MNWs were characterized by scanning electron microscopy (SEM). For example, an SEM cross section of AAO shows that Co MNWs were grown uniformly, Figure 1. MNW lengths of 14, 28, and 2.3 μm were used for Fe, Co, and Ni MNWs, respectively. Figure 2 shows the hysteresis loops of these samples, as obtained by vibrating sample magnetometry (VSM). The saturation magnetization of Fe, Co, and Ni MNWs were 142.6 memu, 232.9 memu, and 5.2 memu, respectively. The coercivities were determined with the field applied parallel and perpendicular to the MNW long axes: 1.16 kOe and 0.1 kOe for Fe, 1.52 kOe and 0.21 kOe for Co, and 0.22 kOe and 0.14 kOe for Ni.

FMR Behavior of Fe, Co, and Ni MNWs. The Kittel equation describes a precessional frequency of magnetic moments, depending on the orientation of the magnetic material and the strength of an applied DC magnetic field,[30,42,48]

$$\left(\frac{\omega}{\gamma}\right)^2 = [H\cos(\theta - \theta_H) + H_{eff}\cos 2\theta][H\cos(\theta - \theta_H) + H_{eff}\cos^2\theta] \quad (1)$$

where ω is the angular frequency ($\omega = 2\pi f$), γ is the gyromagnetic ratio ($\gamma = \frac{g\mu_B}{\hbar}$, where g is the g-factor, μ_B is the Bohr magneton, and $\hbar$ is the reduced Planck constant), H is the applied DC field, H_{eff} is the effective field of MNWs, θ is the angle between magnetization direction and MNW axis, and θ_H is the angle between the applied DC field and MNW axis as shown in Figure 3a.

Here, H_{eff} is briefly defined as the sum of shape anisotropy field, magnetocrystalline anisotropy field, magnetoelastic anisotropy field, and magnetostatic interaction field. However, due to the large aspect ratio of MNWs, the shape anisotropy is dominant and the magnetocrystalline and magnetoelastic anisotropies are negligible at room temperature.[30,31,45] Magnetostatic interactions among MNWs are dependent on

https://doi.org/10.1021/acsanm.1c00086
ACS Appl. Nano Mater. 2021, 4, 3557−3564

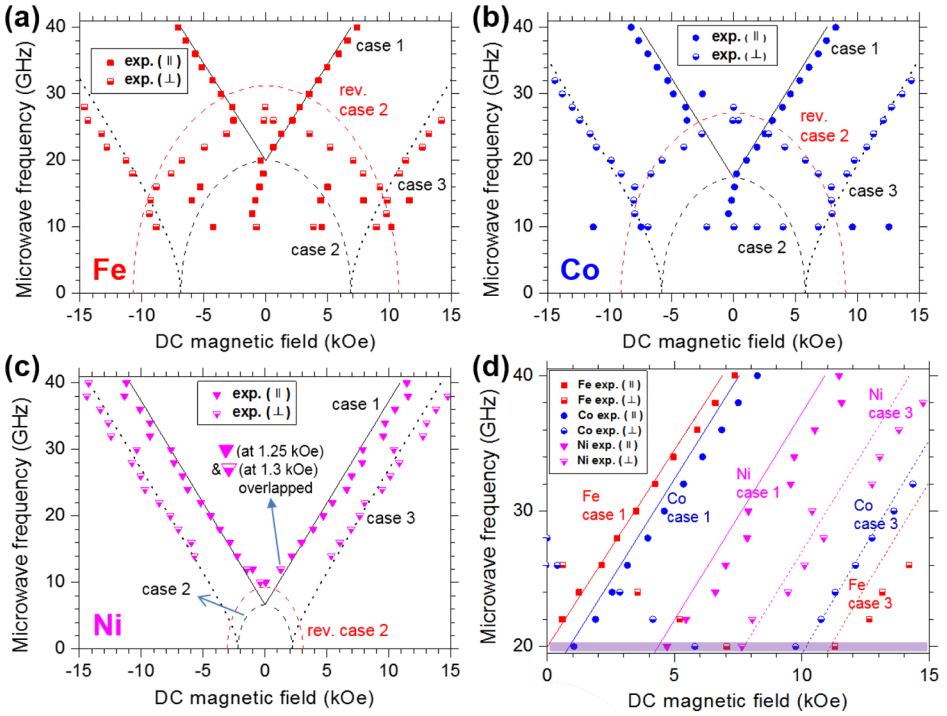

Figure 4. FMR trends of (a) Fe, (b) Co, and (c) Ni MNWs plotted with the Kittel equation for case 1 (black solid lines), case 2 (black dashed lines), revised case 2 (red dashed lines), and case 3 (black dotted lines). (d) FMR trends of Fe, Co, and Ni plotted together in the range of 0−15 kOe and 20−40 GHz. The purple box is for reference purpose for discussion in the text and in Figure 5.

the interwire distances relative to the MNW diameters,[31] which means it is proportional to a fill factor (= a porosity of templates) in our samples. Specifically, the effective field for an array of MNWs, considering shape anisotropy and magnetostatic interactions, is given by $H_{eff} = 2\pi M_s(1-3P)$, where M_s is the saturation magnetization and P is the porosity of the template in which MNWs are grown.[37] This can be confirmed by checking the extreme cases where $H_{eff} = 2\pi M_s$ for $P = 0$ (single nanowires) and $H_{eff} = -4\pi M_s$ for $P = 1$ (films).[30,31] The values of H_{eff} in this work are positive since our fill factors were 12% for Fe and Co MNW samples and 9% for Ni MNW sample.

In the orientations shown in Figure 3a, there are three cases for FMR measurements:[42]

$$\text{case (1)}\ \frac{\omega}{\gamma} = H + H_{eff}$$

(H parallel to MNW axis, $H > 0$, $\theta = 0°$, $\theta_H = 0°$) (2)

$$\text{case (2)}\ \left(\frac{\omega}{\gamma}\right)^2 = {H_{eff}}^2 - H^2$$

(H perpendicular to MNW axis, $0 < H < H_{eff}$, $0 < \theta < 90°$, $\theta_H = 90°$) (3)

$$\text{case (3)}\ \left(\frac{\omega}{\gamma}\right)^2 = H(H - H_{eff})$$ (H perpendicular to MNW axis, $0 < H_{eff} < H$, $\theta = 90°$, $\theta_H = 90°$) (4)

Generally, the remanent magnetization direction of MNWs is along the MNW axis due to the shape anisotropy. If a DC field is applied perpendicular to MNWs, but it is weaker than H_{eff}, the magnetization angle remains between 0 and 90°. However, the magnetization angle changes to 90° when a perpendicular DC field is stronger than H_{eff}. Therefore, the boundary between cases 2 and 3 is the magnitude of H_{eff}. Figure 3b,c shows normalized S_{21} from FMR measurements (observation of the microwave energy absorption due to FMR as a reduction of the transmitted microwave signal, S_{21}, i.e., the ratio of output voltage in port 2 and input voltage in port 1) of Fe MNWs with parallel and perpendicular orientations, respectively.

In Figure 3b, the FMR measurements of Fe MNWs with a parallel orientation shows that the resonant frequency increased as the DC field increased in accordance with eq 2. At each frequency, the microwave signal is absorbed at two different DC fields that are almost symmetric about the origin except at 20 and 24 GHz. The signal at 20 GHz has only one absorption null as expected by the Kittel equation. The signal at 24 GHz seems to have two absorptions: one obvious null at about 1.3 kOe and another shoulder at about −2.5 kOe. The absorption difference between these nulls can be attributed to the remanence in the ferromagnetic material since the field is being swept from positive to negative values. Once the resonant field is more negative than the coercivity (see Figure 2), all of the MNW samples are switched "down", so this absorption difference diminishes. This occurred for both Fe and Co MNWs.

Figure 4 shows the location of the FMR absorption field−frequency pairs for Fe, Co, and Ni MNWs and compares the results with the Kittel equations. The solid (case 1) and dashed (cases 2 and 3) lines are based on eqs 2−4, respectively. The solid and half-solid symbols are the experimental FMR trends

https://doi.org/10.1021/acsanm.1c00086
ACS Appl. Nano Mater. 2021, 4, 3557−3564

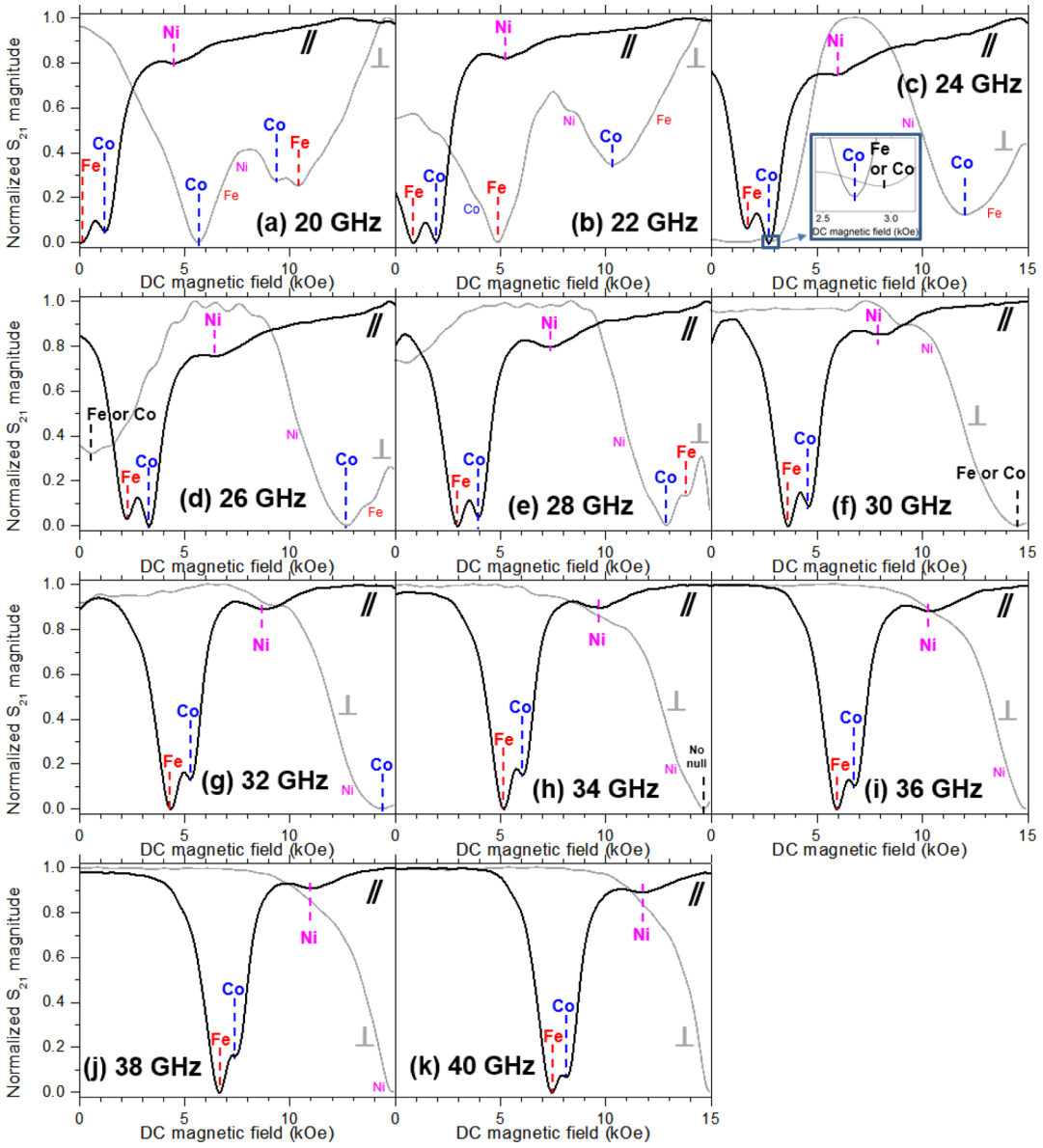

Figure 5. (a–k) Normalized S_{21} (microwave signal at the output compared to the input) at labeled frequencies from combined sample (Fe, Co, and Ni MNWs) measurement with the DC field parallel (black solid line) and perpendicular (gray solid line) to MNW axes.

from FMR measurements with parallel and perpendicular orientations, respectively. Bulk Fe, Co, and Ni have saturation moments of M_s = 1707, 1440, and 485 emu/cm^3 and g-factors = 2.08, 2.145, and 2.185, respectively.[49] The MNW samples made by electrodeposition have nanosized polycrystalline structures.[13,24] Also, as mentioned above, the magnetocrystalline anisotropy field is negligible for Fe and Ni because they have cubic crystal structures. However, the magnetocrystalline anisotropy of hexagonal Co is similar in magnitude to the shape anisotropy because it is uniaxial. To minimize this effect, face-centered cubic Co MNWs were made using a pH = 2 electrolyte,[33−35,37] which has been shown to disturb the crystallization with a high concentration of hydrogen absorbed and desorbed during deposition.[34]

The experimental FMR trends for all parallel orientations (Fe above 20 GHz, Co above 18 GHz, and Ni above 10 GHz) match well with case 1. This means that materials properties such as saturation magnetization and crystal structure (e.g., fcc Co) are accurately measured with FMR[33] and that the effective field, $H_{eff} = 2\pi M_s(1-3P)$ in eq 2, is valid. Therefore, these samples have the predicted magnetostatic interactions, which is also supported by the high (but not saturated) remanent magnetization from the hysteresis loops taken with the field parallel to the MNW axes in Figure 2a. Above the parallel saturation field for each MNW sample (~3 kOe for Fe, ~4 kOe for Co, and ~2 kOe for Ni as shown in Figure 2a), the samples behave as single domains with uniform mode resonance as shown in Figure 4a–c. At these fields, the magnetizations of the MNWs are fully aligned with the DC field. There is an unexpected Co FMR at −2.5 kOe (this field is close to the coercivity and below the saturation field) at 30 GHz because the magnetic domains are not in a single-domain state. Below those frequencies (20 GHz for Fe, 18 GHz for Co, and 10 GHz for Ni), FMR is not defined by the Kittel equation.

On the other hand, the experimental FMR trends of Fe and Co with perpendicular orientation do not follow the case 2 of the Kittel equation. By definition, case 2 is below the saturation

https://doi.org/10.1021/acsanm.1c00086
ACS Appl. Nano Mater. 2021, 4, 3557−3564

field (~9.8 kOe for Fe, ~8 kOe for Co, and ~4 kOe for Ni as shown in Figure 2b), so there is a multidomain state and the magnetostatic interactions between the MNWs are small.[30] This can be confirmed with very low remanence from the perpendicular hysteresis loops of MNWs as shown in Figure 2b. This also means that the resonant frequency is sensitive to magnetostatic interactions for perpendicular orientations. So, for MNW FMR case 2, a revised $H_{eff} = 2\pi M_s$ can be used because the shape anisotropy field (also called the demagnetizing field) is dominant. When this revised H_{eff} is used in eq 3, it yields the red dashed lines in Figure 4a−c. This new case 2 (red dashed lines), together with the previous case 2 (black dashed lines), provides limits for how the magnetostatic interactions affect the resonant frequency. In Figure 4a,b, there appear to be more interactions between Fe MNWs than Co, for example. Case 2 for Ni is below our measurement frequencies.

The experimental FMR trend of Ni with a perpendicular orientation accords closely with case 3 Kittel equation, eq 4. The FMR trends of Fe and Co with perpendicular orientation also correspond to case 3 above perpendicular saturating applied fields at equal to or higher than 18 GHz in Figure 4a,b. This shows that above the saturation field, the MNWs have the expected magnetostatic interactions based on the effective field, $H_{eff} = 2\pi M_s(1-3P)$ as described above.

At 10 GHz, undefined absorption nulls at −0.75 kOe for Fe and at −2.15, 0.05, and 1.9 kOe for Co are detected, in addition to FMR pairs following the original case 2 (3.85 kOe for Fe and 4 kOe for Co) and case 3 (−8.85 and 8.95 kOe for Fe and −6.9 and 6.85 kOe for Co) below the saturation field. All these including unpredicted absorption nulls with parallel orientation below 20 GHz for Fe and 18 GHz for Co result from the unsaturated state (below the saturation field) but will be studied in the future for clarity.

Overall, the FMR trends are well fitted to the Kittel equation. Small differences between the FMR experimental and analytical results could be caused by a small angular variation of the MNW orientation inside the porous templates and/or a misalignment in the experimental setup.[30]

By comparing the FMR measurements and the Kittel equations (Figure 4a−c), it is possible to identify the specific type of MNW used for labeling. Also, it is possible to identify which MNWs and measurements are best used in an FMR-ID system.

Optimization of FMR Measurements for the FMR-ID Labeling System. For efficient labeling and identification, the fundamentals of MNW labeling and FMR-ID detection can be established using the measurement results in Figure 4a−c. Three features in particular stand out. (1) Negative DC field sweeping is not necessary because the FMR trends are symmetric about the origin. FMR trends in positive DC fields from 0 to 15 kOe are sufficient for identification. (2) It is best to use obvious and predictable FMR (absorption nulls that follow the Kittle equations) which occurs for all of the MNWs studied at frequency−field pairs above saturation, or ≥20 GHz. (3) Geometric cases 1 and 3 are best for identification applications because all of the MNW materials have distinct FMR absorption nulls at each frequency.

To verify this hypotheses, three samples were measured together to test the feasibility of MNW-based identification systems. Figure 5 shows the normalized FMR measurements at 20−40 GHz for a combined Fe, Co, and Ni MNW sample with DC field parallel (black solid line) and perpendicular (gray solid line) to the MNW axis. The FMR absorption nulls are labeled corresponding to the FMR individual samples measured in Figure 4d. Also, missing nulls based on the individual measurements are marked in a smaller font at their expected positions. When the applied field is parallel to the MNWs, the three expected absorption nulls are observed at every frequency. On the other hand, the absorption nulls are not as obvious with perpendicularly orientated DC fields. For example, at 20 GHz (corresponding to the purple box in Figure 4d), there are no absorption nulls for Fe (at ~7 kOe) and Ni (at ~7.7 kOe), Figure 5a. Also, the null from Ni (at ~8 kOe) appears only as a shoulder at 22 GHz in Figure 5b. Other absorption nulls with perpendicularly applied fields are so broad that they overlap and it is hard to distinguish them at ~3 kOe and ~14.5 kOe as in Figure 5c,f, respectively. These broad nulls might be caused by small absorption differences and broad linewidths. (For reference, the null at ~14.6 kOe with perpendicular orientation at 34 GHz in Figure 5h is not real absorption but was from curve fitting when there was no data above 15 kOe.)

It should be noted that the null position difference between Fe and Co with the parallel applied DC field is only about 1 kOe but they are always distinguishable. However, measurements with perpendicular DC applied fields do not show all distinguishable nulls even when the null position difference is more than 1 kOe. It seems that the field linewidth of the FMR absorption with parallel DC fields is narrower than that with perpendicular DC fields. Another interesting feature is that FMR measurements with parallel DC fields only show three nulls, rather than five nulls with perpendicular DC fields from 20 to 26 GHz, as expected by Figures 4d and 5a−d. The five perpendicular nulls consist of two nulls from case 2 FMR and three nulls from case 3 FMR. The case 2 FMR absorption can be located anywhere between the original and the modified case 2 theoretical lines, as shown in Figure 4a,b, depending on the presence of magnetostatic interactions between the MNWs. In other words, it will be hard to recognize, for example, which FMR null belongs to Fe or Co. So, case 2 FMR is not very reliable for FMR-ID. Also, the three nulls (Fe, Co, and Ni) from the case 3 FMR in Figure 4a−c disappear as the microwave frequency increases, which would make reliable FMR-ID difficult. Higher DC fields would be necessary to get enough data with perpendicularly oriented DC fields. For the reasons above, case 1 FMR (absorption nulls and their trends) appear to be the best geometry for efficient FMR-ID detection.

A summary of these nulls from Figure 5 is plotted in Figure 6. At 22 GHz, the Fe FMR absorption was at 0.85 kOe, Co at 1.95 kOe, and Ni at 5.25 kOe. These same materials had FMR at 0.6 kOe, 1.9 kOe, and 5.45 kOe when measured individually at this frequency. Also, the Fe FMR null at 20 GHz was observed at ~0.1 kOe in this combined measurement but was absent when measured individually. Another change in the null position was found with perpendicular orientation at 28 GHz in Figure 5e as Fe FMR appeared at ~13.9 kOe but was not present in the individual measurement. The combined sample measurement showed other little shifts in the FMR absorption null locations as well. The little shifts could result from the magnetostatic interactions among samples caused by stacking. Despite these minor discrepancies, all three absorption nulls are obvious in all of the results with parallel DC applied fields from 20 to 40 GHz, as shown in Figure 5. In general, the FMR absorption nulls and trends from the combined and individual sample measurements are similar, as shown in Figure 6, and all

https://doi.org/10.1021/acsanm.1c00086
ACS Appl. Nano Mater. 2021, 4, 3557−3564

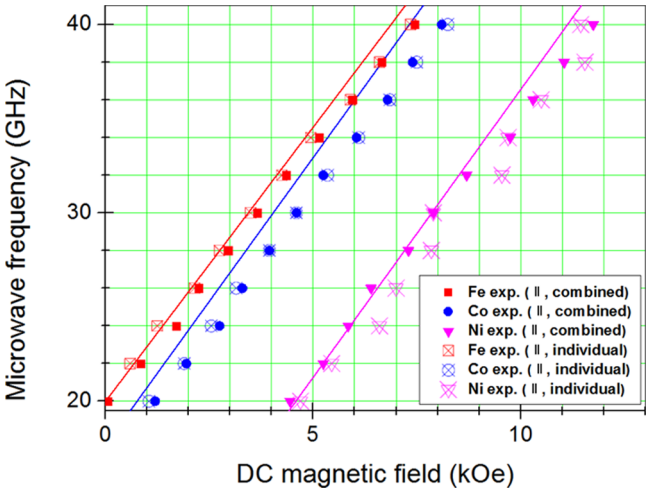

Figure 6. FMR trends from combined (solid symbol) and individual (empty crossed symbol) sample measurements with parallel orientation in the range of 0−13 kOe and 20−40 GHz with the case 1 Kittel equation (solid lines).

three of the FMR-ID labels would have been correctly identified in an FMR-ID application.

Importantly, every ferromagnetic material has its own FMR behavior as a fingerprint. Theoretically, ferromagnetic alloys or multilayered structures could be incorporated into MNWs for a variety of unique signatures for FMR-ID,[50] which are comparable to spectrally resolvable fluorophores used currently for cell sorting and identification.[21] In fact, if the FMR and fluorescence techniques were used together, it could be a strong potential labeling technique.

CONCLUSIONS

To verify the potential of an FMR-ID labeling system, Fe, Co, and Ni MNW samples were fabricated by template-assisted pulsed electrodeposition and measured for FMR absorption individually and in combination. For FMR analysis, the Kittel equation was generally used, but in order to better understand the FMR behavior of MNW samples with a perpendicular orientation, the Kittel equation had to be revised. FMR analysis provided a good estimation of the magnetic properties in the MNW system, such as the saturation magnetization, the magnetostatic interaction field, and the shape anisotropy field. Generally, regardless of MNW sample's orientation, the MNW system was in a single-domain state above the saturation field or in a multidomain state below the saturation field. The parallel MNW-DC field orientation (case 1 FMR) with the optimized ranges of DC field (positive DC field from 0 to 15 kOe) and microwave frequency (at 20 GHz or above) was shown to yield the most efficient FMR-ID detection. Both individual and combined FMR measurements show the potential of the MNW-based FMR-ID labeling system, which can also be applied to the current cell-labeling techniques.

EXPERIMENTAL METHODS

Nanowire Fabrication. Fe, Co, and Ni nanowires were used in this work. Nanowires were made in porous anodic aluminum oxide (AAO) and track-etched polycarbonate (TEPC) by pulsed-electrodeposition using a three-electrode system at room temperature. The AAO templates (40 nm pore diameter, 12% porosity, and 50 μm thickness) and the TEPC membranes (200 nm pore diameter, 9% porosity, and 10 μm thickness) were obtained from InRedox and GE Healthcare, respectively. Prior to electrodeposition, 7 nm of titanium and 500 nm of copper were sputtered on one side of the AAO (for Fe and Co) or TEPC (for Ni) for adhesion and electric contact for electrodeposition, respectively. A thin platinum mesh was used as the counter electrode. Fe MNWs were fabricated from a solution of 0.55 mol $FeSO_4$, 0.73 mol H_3BO_3, and 5.68 mmol $C_6H_8O_6$ (pH = 3) at a pulsed-potential of $V = -1.1$ V versus Ag/AgCl. Co MNWs (face-centered cubic Co for the minimum effect of the magnetocrystalline anisotropy, which is discussed in Results and Discussion section) were made from a solution of 0.85 mol $CoSO_4$ and 0.48 mol H_3BO_3 (pH = 2) at a pulsed-potential of $V = -0.95$ V versus Ag/AgCl. Ni MNWs were deposited from a solution of 0.85 mol $NiSO_4$, 0.17 mol $NiCl_2$, and 0.65 mol H_3BO_3 (pH = 2.5) at a pulsed-potential of $V = -0.9$ V versus Ag/AgCl. The pH of the solutions was adjusted using diluted H_2SO_4 and NaOH. The wire lengths were controlled by counting the deposited charge, which indicates the volume of material deposited in pores.

Nanowire Length Characterization. The length of MNWs was measured using a JEOL 6500F scanning electron microscope. The beam was set to 25 kV with medium probe current available.

Magnetic Measurements. The hysteresis curves (+10 kOe to −10 kOe) of MNWs were measured at room temperature using Princeton and Lakeshore vibrating sample magnetometers.

FMR Measurements. For FMR measurements, a VNA (Anritsu 37369D) was used to apply and detect microwave signals with nonmagnetic connectors and cables to avoid interference from other magnetic materials.[15,23] The microwave signal induces an ac magnetic field. As shown in Figure 7a, a 50 Ω coplanar waveguide (CPW) board was designed on 10 mi Duroid 5880LZ ($\varepsilon_r = 2$) with a signal line width of 16.5 mi, signal line length of 6.8 cm, gap width of 5 mi, and 2.4 mm nonmagnetic end launch connectors.[23] This CPW board

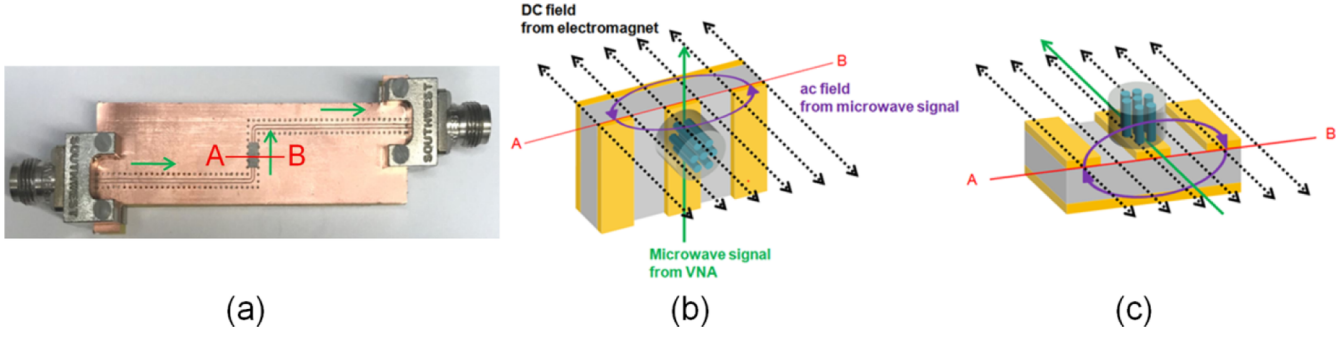

Figure 7. (a) Photo of a CPW board with the Co MNW sample (gray rectangle). Green arrows show the direction of the microwave current and the line A-B shows the orientation of the magnetic field. (b,c) Schematic, not to scale, showing the orientations of the sample and both ac (purple ellipses) and DC (black lines) magnetic fields. The CPW board was rotated such that the DC field was (b) parallel or (c) perpendicular to the MNW axes.

https://doi.org/10.1021/acsanm.1c00086
ACS Appl. Nano Mater. 2021, 4, 3557−3564

was used to provide an ac magnetic field that was perpendicular to the MNW axes, Figure 7b,c, while an electromagnet provided a DC magnetic field either parallel or perpendicular to the MNW axes. FMR measurements were performed using a sweeping DC field from +15 kOe to −15 kOe at constant ac frequencies from 10 to 40 GHz with 2 GHz intervals. At specific field−frequency pairs, MNWs absorbed the microwave energy due to FMR. This absorption was observed by the VNA as a reduction of the transmitted microwave signal (S_{21}, the ratio of output voltage in port 2 and input voltage in port 1). The transmitted microwave signals were normalized and analyzed.

■ ASSOCIATED CONTENT

Supporting Information

The Supporting Information is available free of charge at https://pubs.acs.org/doi/10.1021/acsanm.1c00086.

Normalized S_{21} from FMR measurements of Fe, Co, and Ni MNWs and error analysis of S_{21} and *g*-factor (PDF)

■ AUTHOR INFORMATION

Corresponding Authors

Joseph Um − *Department of Electrical and Computer Engineering, University of Minnesota, Minneapolis, Minnesota 55455, United States;* orcid.org/0000-0002-9833-4943; Email: umxxx023@umn.edu

Bethanie J. H. Stadler − *Department of Electrical and Computer Engineering, University of Minnesota, Minneapolis, Minnesota 55455, United States*; Email: stadler@umn.edu

Authors

Yali Zhang − *Department of Electrical and Computer Engineering, University of Minnesota, Minneapolis, Minnesota 55455, United States*

Wen Zhou − *Department of Electrical and Computer Engineering, University of Minnesota, Minneapolis, Minnesota 55455, United States*

Mohammad R. Zamani Kouhpanji − *Department of Electrical and Computer Engineering, University of Minnesota, Minneapolis, Minnesota 55455, United States;* orcid.org/0000-0002-3042-9997

Cosmin Radu − *Lake Shore Cryotronics Inc, Westerville 43082, Ohio, United States*

Rhonda R. Franklin − *Department of Electrical and Computer Engineering, University of Minnesota, Minneapolis, Minnesota 55455, United States*

Complete contact information is available at: https://pubs.acs.org/10.1021/acsanm.1c00086

Notes

The authors declare no competing financial interest.

■ ACKNOWLEDGMENTS

This work was supported by the National Science Foundation under award number CMMI-1762884. Parts of this work were carried out in the Characterization Facility and the Minnesota Nano Center at the University of Minnesota, which received partial support from the NSF through the MRSEC and the National Nano Coordinated Infrastructure Network (NNCI award number ECCS-2025124) programs, respectively, and at the Institute for Rock Magnetism (IRM) at the University of Minnesota. The IRM is a U.S. National Multi-user Facility supported through the Instrumentation and Facilities program of the National Science Foundation, Earth Sciences Division, and by funding from the University of Minnesota.

■ REFERENCES

(1) Pathak, R.; Joshi, S. Multi-Scale Modeling and Analysis of Nano-RFID Systems on HPC Setup. In *Contemporary Computing*; Ranka, S., Aluru, S., Buyya, R., Chung, Y.-C., Dua, S., Grama, A., Gupta, S. K. S., Kumar, R., Phoha, V. V., Eds.; Springer Berlin Heidelberg: Berlin, Heidelberg, 2009; pp 649−659.

(2) Kim, J.; Wang, Z.; Kim, W. S. Stretchable RFID for Wireless Strain Sensing With Silver Nano Ink. *IEEE Sens. J.* **2014**, *14*, 4395−4401.

(3) Singh, R.; Singh, E.; Nalwa, H. S. Inkjet Printed Nanomaterial Based Flexible Radio Frequency Identification (RFID) Tag Sensors for the Internet of Nano Things. *RSC Adv.* **2017**, *7*, 48597−48630.

(4) Farokhzad, O. C.; Langer, R. Impact of Nanotechnology on Drug Delivery. *ACS Nano* **2009**, *3*, 16−20.

(5) Kumar, C. S. S. R.; Mohammad, F. Magnetic Nanomaterials for Hyperthermia-Based Therapy and Controlled Drug Delivery. *Adv. Drug Delivery Rev.* **2011**, *63*, 789−808.

(6) Laurent, S.; Dutz, S.; Häfeli, U. O.; Mahmoudi, M. Magnetic Fluid Hyperthermia: Focus on Superparamagnetic Iron Oxide Nanoparticles. *Adv. Colloid Interface Sci.* **2011**, *166*, 8−23.

(7) Park, J. H.; Yang, S. H.; Lee, J.; Ko, E. H.; Hong, D.; Choi, I. S. Nanocoating of Single Cells: From Maintenance of Cell Viability to Manipulation of Cellular Activities. *Adv. Mater.* **2014**, *26*, 2001−2010.

(8) Liu, C.; Stakenborg, T.; Peeters, S.; Lagae, L. Cell Manipulation with Magnetic Particles toward Microfluidic Cytometry. *J. Appl. Phys.* **2009**, *105*, 102014.

(9) Nemati, Z.; Zamani Kouhpanji, M. R.; Zhou, F.; Das, R.; Makielski, K.; Um, J.; Phan, M.-H.; Muela, A.; Fdez-Gubieda, M. L.; Franklin, R. R.; Stadler, B. J. H.; Modiano, J. F.; Alonso, J. Isolation of Cancer-Derived Exosomes Using a Variety of Magnetic Nanostructures: From Fe3O4 Nanoparticles to Ni Nanowires. *Nanomaterials* **2020**, *10*, 1662.

(10) Lewis, J. K.; Bischof, J. C.; Braslavsky, I.; Brockbank, K. G. M.; Fahy, G. M.; Fuller, B. J.; Rabin, Y.; Tocchio, A.; Woods, E. J.; Wowk, B. G.; Acker, J. P.; Giwa, S. The Grand Challenges of Organ Banking: Proceedings from the First Global Summit on Complex Tissue Cryopreservation. *Cryobiology* **2016**, *72*, 169−182.

(11) Khosla, K.; Wang, Y.; Hagedorn, M.; Qin, Z.; Bischof, J. Gold Nanorod Induced Warming of Embryos from the Cryogenic State Enhances Viability. *ACS Nano* **2017**, *11*, 7869−7878.

(12) Rao, W.; Huang, H.; Wang, H.; Zhao, S.; Dumbleton, J.; Zhao, G.; He, X. Nanoparticle-Mediated Intracellular Delivery Enables Cryopreservation of Human Adipose-Derived Stem Cells Using Trehalose as the Sole Cryoprotectant. *ACS Appl. Mater. Interfaces* **2015**, *7*, 5017−5028.

(13) Shore, D.; Ghemes, A.; Dragos-Pinzaru, O.; Gao, Z.; Shao, Q.; Sharma, A.; Um, J.; Tabakovic, I.; Bischof, J. C.; Stadler, B. J. H. Nanowarming using Au-tipped Co35Fe65 ferromagnetic nanowires. *Nanoscale* **2019**, *11*, 14607−14615.

(14) Safronov, A. P.; Stadler, B. J. H.; Um, J.; Zamani Kouhpanji, M. R.; Alonso Masa, J.; Galyas, A. G.; Kurlyandskaya, G. V. Polyacrylamide Ferrogels with Ni Nanowires. *Materials* **2019**, *12*, 2582.

(15) Zhou, W.; Um, J.; Stadler, B.; Franklin, R. Design of Self-Biased Coplanar Circulator with Ferromagnetic Nanowires. *2018 IEEE Radio and Wireless Symposium (RWS)*; IEEE: Anaheim, CA, 2018; pp 240−242.

(16) Stadler, B.; Reddy, M.; Basantkumar, R.; McGary, P.; Estrine, E.; Huang, X.; Sung, S.; Tan, L.; Zou, J.; Maqableh, M.; Shore, D.; Gage, T.; Um, J.; Hein, M.; Sharma, A. Galfenol Thin Films and Nanowires. *Sensors* **2018**, *18*, 2643.

(17) Um, J.; Park, J. J.; Flatau, A.; Zhou, W.; Zhang, Y.; Franklin, R.; Reddy, K. S. M.; Tan, L.; Sharma, A.; Sung, S.-Y.; Zou, J.; Stadler, B. 22 - Template-Assisted Electrodeposited Magnetic Nanowires and Their Properties for Applications. In *Magnetic Nano- and Microwires*, 2 ed; Vázquez, M., Ed.; Woodhead Publishing Series in Electronic and Optical Materials; Woodhead Publishing, 2020; pp 675−695.

(18) Pondman, K. M.; Maijenburg, A. W.; Celikkol, F. B.; Pathan, A. A.; Kishore, U.; Haken, B. t.; ten Elshof, J. E. Au Coated Ni

Nanowires with Tuneable Dimensions for Biomedical Applications. *J. Mater. Chem. B* **2013**, *1*, 6129.
(19) Sharma, A.; Orlowski, G. M.; Zhu, Y.; Shore, D.; Kim, S. Y.; DiVito, M. D.; Hubel, A.; Stadler, B. J. H. Inducing Cells to Disperse Nickel Nanowires via Integrin-Mediated Responses. *Nanotechnology* **2015**, *26*, 135102.
(20) Salem, A. K.; Searson, P. C.; Leong, K. W. Multifunctional Nanorods for Gene Delivery. *Nat. Mater.* **2003**, *2*, 668−671.
(21) Sharma, A.; Zhu, Y.; Thor, S.; Zhou, F.; Stadler, B.; Hubel, A. Magnetic Barcode Nanowires for Osteosarcoma Cell Control, Detection and Separation. *IEEE Trans. Magn.* **2013**, *49*, 453−456.
(22) Sharma, A.; DiVito, M. D.; Shore, D. E.; Block, A. D.; Pollock, K.; Solheid, P.; Feinberg, J. M.; Modiano, J.; Lam, C. H.; Hubel, A.; Stadler, B. J. H. Alignment of Collagen Matrices Using Magnetic Nanowires and Magnetic Barcode Readout Using First Order Reversal Curves (FORC) (Invited). *J. Magn. Magn. Mater.* **2018**, *459*, 176−181.
(23) Zhou, W.; Um, J.; Zhang, Y.; Nelson, A. P.; Nemati, Z.; Modiano, J.; Stadler, B.; Franklin, R. Development of a Biolabeling System Using Ferromagnetic Nanowires. *IEEE J. Electromagn. RF Microw. Med. Biol.* **2019**, *3*, 134−142.
(24) Reddy, S. M.; Park, J. J.; Na, S.-M.; Maqableh, M. M.; Flatau, A. B.; Stadler, B. J. H. Electrochemical Synthesis of Magnetostrictive Fe-Ga/Cu Multilayered Nanowire Arrays with Tailored Magnetic Response. *Adv. Funct. Mater.* **2011**, *21*, 4677−4683.
(25) Zamani Kouhpanji, M. R.; Um, J.; Stadler, B. J. H. Demultiplexing of Magnetic Nanowires with Overlapping Signatures for Tagged Biological Species. *ACS Appl. Nano Mater.* **2020**, *3*, 3080−3087.
(26) Rodbell, D. S. Ferromagnetic Resonance of Iron Whisker Crystals. *J. Appl. Phys.* **1959**, *30*, S187−S188.
(27) Kambersky, V. Ferromagnetic Resonance in Iron Whiskers. *Can. J. Phys.* **1970**, *48*, 1103−1104.
(28) Heinrich, B.; Arrott, A. S. Low Field Ferromagnetic Resonance in Iron Whiskers near Tc. *J. Magn. Magn. Mater.* **1983**, *31-34*, 669−671.
(29) Ebels, U.; Duvail, J.-L.; Wigen, P. E.; Piraux, L.; Buda, L. D.; Ounadjela, K. Ferromagnetic Resonance Studies of Ni Nanowire Arrays. *Phys. Rev. B: Condens. Matter Mater. Phys.* **2001**, *64*, 228−233.
(30) Encinas-Oropesa, A.; Demand, M.; Piraux, L.; Huynen, I.; Ebels, U. Dipolar Interactions in Arrays of Nickel Nanowires Studied by Ferromagnetic Resonance. *Phys. Rev. B: Condens. Matter Mater. Phys.* **2001**, *63*, 104415.
(31) Demand, M.; Encinas-Oropesa, A.; Kenane, S.; Ebels, U.; Huynen, I.; Piraux, L. Ferromagnetic Resonance Studies of Nickel and Permalloy Nanowire Arrays. *J. Magn. Magn. Mater.* **2002**, *249*, 228−233.
(32) Yalçın, O.; Yıldız, F.; Özdemir, M.; Aktaş, B.; Köseoğlu, Y.; Bal, M.; Tuominen, M. T. Ferromagnetic Resonance Studies of Co Nanowire Arrays. *J. Magn. Magn. Mater.* **2004**, *272−276*, 1684−1685.
(33) Darques, M.; Encinas, A.; Vila, L.; Piraux, L. Controlled Changes in the Microstructure and Magnetic Anisotropy in Arrays of Electrodeposited Co Nanowires Induced by the Solution PH. *J. Phys. D: Appl. Phys.* **2004**, *37*, 1411−1416.
(34) Darques, M.; Piraux, L.; Encinas, A. Influence of the Diameter and Growth Conditions on the Magnetic Properties of Cobalt Nanowires. *IEEE Trans. Magn.* **2005**, *41*, 3415−3417.
(35) Darques, M.; Bogaert, A.-S.; Elhoussine, F.; Michotte, S.; Medina, J. d. l. T.; Encinas, A.; Piraux, L. Controlled Growth of CoCu Nanowires and Application to Multilayered CoCu/Cu Nanowires with Selected Anisotropy. *J. Phys. D: Appl. Phys.* **2006**, *39*, 5025−5032.
(36) Yamaguchi, A.; Motoi, K.; Hirohata, A.; Miyajima, H.; Miyashita, Y.; Sanada, Y. Broadband ferromagnetic resonance ofNi81Fe19wires using a rectifying effect. *Phys. Rev. B: Condens. Matter Mater. Phys.* **2008**, *78*, 104401.
(37) Darques, M.; Spiegel, J.; De la Torre Medina, J.; Huynen, I.; Piraux, L. Ferromagnetic Nanowire-Loaded Membranes for Microwave Electronics. *J. Magn. Magn. Mater.* **2009**, *321*, 2055−2065.
(38) Kartopu, G.; Yalçın, O.; Kazan, S.; Aktaş, B. Preparation and FMR Analysis of Co Nanowires in Alumina Templates. *J. Magn. Magn. Mater.* **2009**, *321*, 1142−1147.
(39) Carignan, L.-P.; Boucher, V.; Kodera, T.; Caloz, C.; Yelon, A.; Ménard, D. Double Ferromagnetic Resonance in Nanowire Arrays. *Appl. Phys. Lett.* **2009**, *95*, 062504.
(40) Kraus, L.; Infante, G.; Frait, Z.; Vázquez, M. Ferromagnetic Resonance in Microwires and Nanowires. *Phys. Rev. B: Condens. Matter Mater. Phys.* **2011**, *83*, 174438.
(41) Yalçın, O. Ferromagnetic Resonance. In *Ferromagnetic Resonance - Theory and Applications*; Yalçın, O., Ed.; InTech, 2013.
(42) Sharma, M.; Pathak, S.; Sharm, M. FMR Measurements of Magnetic Nanostructures. In *Ferromagnetic Resonance - Theory and Applications*; Yalçın, O., Ed.; IntechOpen, 2013.
(43) Yuan, L.; Meng, S.; Shi, Y.; Zhang, Y.; Yue, Z.; Li, L. Dual Band Microwave Ferromagnetic Resonance Absorption in Annealed Cobalt Nanowire Arrays. *Appl. Phys. Lett.* **2014**, *105*, 182407.
(44) Aphesteguy, J.; Jacobo, S.; Lezama, L.; Kurlyandskaya, G.; Schegoleva, N. Microwave Resonant and Zero-Field Absorption Study of Doped Magnetite Prepared by a Co-Precipitation Method. *Molecules* **2014**, *19*, 8387−8401.
(45) Aslam, S.; Khanna, M.; Kuanr, B. K.; Celinski, Z. One dimensional FexCo1-x nanowires; ferromagnetic resonance and magnetization dynamics. *AIP Adv.* **2017**, *7*, 056027.
(46) Kraus, L.; Lynnyk, A.; Azamat, D.; Drahokoupil, J.; Kopeček, J.; Rameš, M. Multi-Peak Ferromagnetic Resonance in Co Nanowires Array. *J. Magn. Magn. Mater.* **2017**, *421*, 241−249.
(47) Zhang, Y.; Um, J.; Zhou, W.; Stadler, B.; Franklin, R. Magnetic Nanowires for RF Applications: Ferromagnetic Resonance and Permeability Characterization. *2019 IEEE MTT-S International Microwave Symposium (IMS)*; IEEE: Boston, MA, USA, 2019; pp 1100−1103.
(48) Kittel, C. On the Theory of Ferromagnetic Resonance Absorption. *Phys. Rev.* **1948**, *73*, 155−161.
(49) Schoen, M. A. W.; Lucassen, J.; Nembach, H. T.; Silva, T. J.; Koopmans, B.; Back, C. H.; Shaw, J. M. Magnetic properties of ultrathin3dtransition-metal binary alloys. I. Spin and orbital moments, anisotropy, and confirmation of Slater-Pauling behavior. *Phys. Rev. B* **2017**, *95*, 134410.
(50) Um, J.; Kouhpanji, M. R. Z.; Liu, S.; Porshokouh, Z. N.; Sung, S.-Y.; Kosel, J.; Stadler, B. Fabrication of Long-Range Ordered Aluminum Oxide and Fe/Au Multilayered Nanowires for 3-D Magnetic Memory. *IEEE Trans. Magn.* **2020**, *56*, 1−6.

https://doi.org/10.1021/acsanm.1c00086
ACS Appl. Nano Mater. 2021, 4, 3557−3564